ACS APPLIED MATERIALS & INTERFACES

Research Article

www.acsami.org

Oxygen Reduction Catalyzed by Au–TiO_2 Nanocomposites in Alkaline Media

Chan Lin,[†,‡] Yang Song,[‡] Lixin Cao,[§] and Shaowei Chen*[,‡]

[†]College of Chemistry and Chemical Engineering, Ocean University of China, Qingdao, Shandong 266100, China

[‡]Department of Chemistry and Biochemistry, University of California, 1156 High Street, Santa Cruz, California 95064, United States

[§]Institute of Materials Science and Engineering, Ocean University of China, Qingdao, Shandong 266100, China

Supporting Information

ABSTRACT: Au–TiO_2 nanocomposites were prepared by chemical deposition of gold nanoparticles onto TiO_2 nanocolloids that were synthesized by a hydrothermal method. Transmission electron microscopic measurements showed that the TiO_2 colloids exhibited an average diameter of about 5 nm and clearly defined lattice fringes that were consistent with those of anatase TiO_2 and formed rather large agglomerates that spanned a few hundred nanometers in length. Additionally, gold nanoparticles were found to be embedded within the TiO_2 matrices, and the size increased with increasing gold loading but all ranged from 10 to 50 nm in diameter. Consistent results were obtained in X-ray diffraction measurements. Electrochemical studies demonstrated that the resulting Au–TiO_2 nanocomposites exhibited apparent electrocatalytic activity in oxygen reduction that was markedly improved as compared to that of TiO_2 particles alone, as reflected in the onset potential, number of electron transfers involved, and kinetic current density. Among the series, the best catalyst for oxygen reduction was identified with the Au/Ti atomic ratio of 5.2%. The enhanced oxygen reduction kinetics was ascribed to the dissociation of water and formation of surface-adsorbed hydroxyl moieties that was facilitated by the loading of gold nanoparticles onto the TiO_2 colloids.

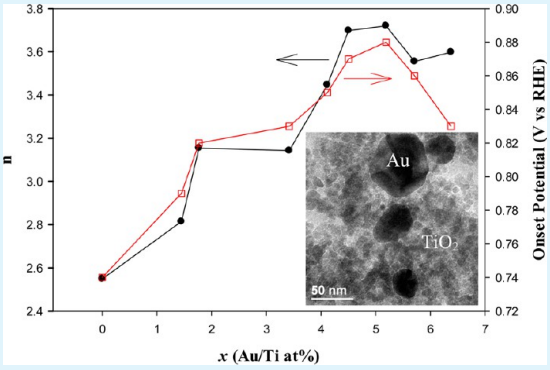

KEYWORDS: *Au–TiO_2 nanocomposite, oxygen reduction, alkaline media, RRDE, Tafel plot*

INTRODUCTION

In fuel cell electrochemistry, efficient catalysts are necessary for both the oxidation of small organic molecule fuels at the anode and oxygen reduction at the cathode to enhance the electron-transfer kinetics and hence produce the current density that is needed for practical applications. Of this, it has long been recognized that the primary bottleneck to fuel cell performance is the oxygen reduction reactions (ORRs). At present, platinum and platinum-based alloy nanoparticles have been examined extensively as the catalysts of choice for ORR because of their well-known high catalytic activity. However, platinum is expensive and of limited reserve. Therefore, in recent years a great deal of attention has been focused on the development of nonplatinum metal catalysts for fuel cell electrochemistry,[1] including transition metal oxides,[2−4] transition metal sulfides,[5] transition metal macrocyclic complexes,[6,7] metal-containing porphyrin systems,[8] etc.

Among these, transition metal oxides are attracting particular attention as efficient electrode catalysts for ORR because of their low cost, abundance, long-term chemical stability, and high photocatalytic activity. For instance, titanium dioxides have been widely used for oxygen reduction in both acidic and alkaline media, though with a high overpotential.[9−13] In one study, Mentus[3] anodically formed TiO_2 in both alkaline and acidic solutions which was found to exhibit apparent electrocatalytic activiy for ORRs. The active sites were proposed to be Ti^{3+} that might be generated voltammetrically. Interestingly, the reactions were observed to follow the direct 4e reduction pathway in alkaline media, whereas in acidic media, the inefficient 2e reduction pathway was favored. However, the onset potential for oxygen reduction was found to be around −0.2 V versus reversible hydrogen electrode (RHE), significantly more negative than the thermodynamic prediction. In another study, Kim et al.[14] prepared titanium oxide by heat treatment of titanium sheets in the temperature range of 600–1000 °C, and the best catalysts were identified as those prepared at 900 °C where ORR occurred at the potential of about +0.65 V versus RHE in 0.1 M H_2SO_4.

Apparently these activities are rather limited. Therefore, to further enhance the electrocatalytic performance, metal oxides are typically doped with a minimal amount of selected metals in the form of nanoparticles, and gold has attracted great interest

Received: September 30, 2013
Accepted: November 11, 2013
Published: November 11, 2013

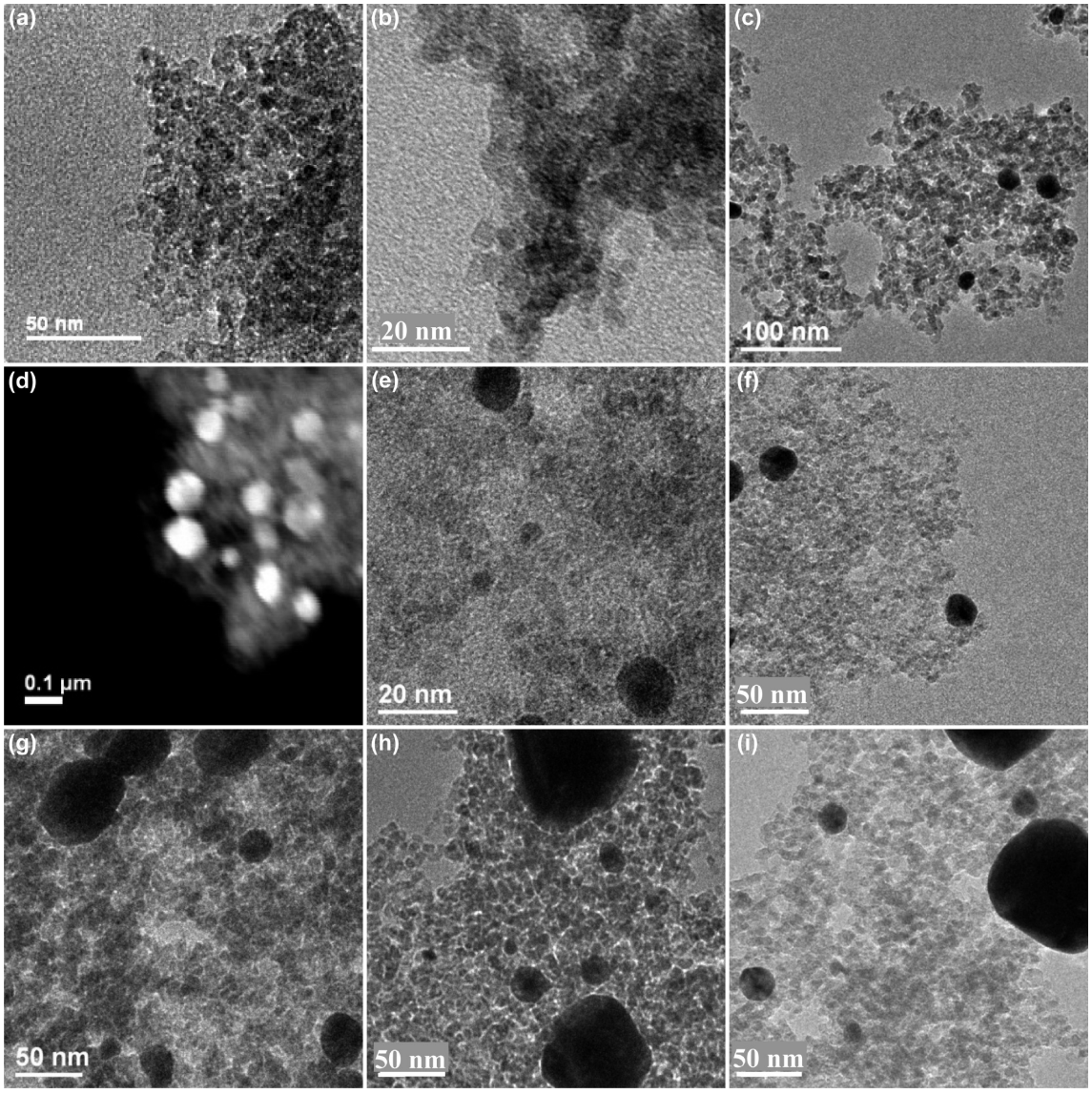

Figure 1. Representative TEM images of Au−TiO_2 (x) nanocomposites at different Au/Ti atomic ratios: (a) x = 0%, (b) x = 1.4%, (c) x = 1.8%, (d) x = 3.4%, (e) x = 4.1%, (f) x = 4.5%, (g) x = 5.2%, (h) x = 5.7%, and (i) x = 6.4%.

in oxygen reduction, in particular in the form of nanoclusters and nanoparticles, where strong metal−support interactions are proposed to account for the enhanced electrocatalytic activity of the resulting Au−TiO_2 composites in oxygen reduction.[15−19] For instance, gold films have been deposited on nanocrystalline anatase titania thin-film surfaces by electron beam deposition, spontaneous displacement reactions, or potentiodynamic polarization,[20,21] and oxygen reduction was found to proceed by the 4e route, as evidenced by the Koutecky−Levich analysis, with the best onset potential close to +0.90 V vs RHE. In another study, Macak et al.[22] prepared TiO_2 nanotube arrays by electrochemical anodization of Ti sheets which were then decorated with gold nanoparticles (3 ± 2 nm). The resulting nanocomposites exhibited a manifold increase of the reaction rate as compared with a flat TiO_2 support or a pure gold electrode. Yet the onset potential for oxygen reduction remained practically unchanged. Thus, much remains to be done with regards to the development of highly efficient Au−TiO_2 nanocomposite catalysts for ORR.

Within this context, in the present study, we prepared a series of Au−TiO_2 nanocomposites by chemically growing gold nanoparticles on TiO_2 nanocolloids at controlled gold loading. Transmission electron microscopy (TEM) and X-ray diffraction (XRD) measurements showed that the TiO_2 colloids were of anatase crystalline structures with an average diameter of about 5 nm, and the gold nanoparticles were deposited onto the TiO_2 agglomerates with the size ranging from 10 to 50 nm. The electrocatalytic activity in oxygen reduction was then evaluated by rotating ring-disk voltammetry, and the best catalyst among the series was identified at a gold/titanium atomic ratio of 5.2%, as manifested by the onset potential, number of electron transfers involved in oxygen reduction, and kinetic current density. The results were accounted for by the formation of adsorbed hydroxy moieties and ultimately the electron-transfer kinetics of oxygen reduction that was facilitated by the loading of gold nanoparticles onto the TiO_2 matrices.

EXPERIMENTAL SECTION

Chemicals. 3-Chloroaniline (99%, ACROS), titanium(IV) *n*-butoxide (99%, ACROS), oleic acid (Fisher Scientific), Nafion 117 solution (Fluka), and L(+)-ascorbic acid (99%, ACROS) were used as received without further treatment. Hydrogen tetrachloroauric acid ($HAuCl_4{\cdot}nH_2O$) was synthesized by dissolving ultrahigh purity gold (99.999%, Johnson Matthey) in freshly prepared aqua regia followed by crystallization.[23] Ultrapure N_2 and O_2 were used for the deaeration of the electrolyte solutions and oxygen reduction reactions, respectively. Water was supplied by a Barnstead Nanopure Water System (18.3 MΩ·cm).

Synthesis of TiO_2 Nanoparticles. The preparation of TiO_2 nanoparticles has been detailed in our previous study.[24] Briefly, 0.1 mL of 3-chloroaniline was added into 10 mL of Nanopure water and then transferred to a Teflon-lined stainless-steel autoclave. Subsequently, 0.17 g of titanium(IV) *n*-butoxide and 1.0 mL of oleic acid were dissolved in 10 mL of toluene and added into the autoclave. The mixed solution was then subject to hydrothermal reactions at 180 °C for 12 h. The white precipitates (TiO_2) were collected and extensively rinsed with methanol.

Synthesis of Au−TiO_2 Nanocomposites. The TiO_2 nanoparticles prepared above were then used for the preparation of Au−TiO_2 nanocomposites. In a typical reaction, the TiO_2 nanoparticles prepared above were dispersed in 15 mL of water along with a calculated amount of $HAuCl_4$. Then the mixed solution was transferred to a Teflon-lined stainless-steel autoclave for hydrothermal reactions at 180 °C for 12 h. After the solution was cooled to room temperature, a calculated amount of ascorbic acid (at a 3:1 molar feed ratio of ascorbic acid to Au) was added into the autoclave, and the solution was subject to a second hydrothermal treatment at 110 °C for 12 h. The resulting purple precipitates were collected by centrifugation and purified by repeated rinsing with Nanopure water. Eight samples were prepared with the Au/Ti atomic ratio (x) of 1.4%, 1.8%, 3.4%, 4.1%, 4.5%, 5.2%, 5.7%, and 6.4%, as determined by the integrated peak areas of the Au 4f and Ti 2p electrons in XPS measurements (Figure S1, in the Supporting Information).

Characterization. Transmission electron microscopy (TEM) studies were carried out with a JOEP JEM-2010 TEM microscope operated at 200 kV. The samples were prepared by suspending the powder sample in toluene and dropcasting onto a Cu grid. X-ray diffraction (XRD) measurements were performed with a Rigaku Miniflew powder diffractometer using Cu Kα radiation with a Ni filter (λ = 0.154059 nm at 30 kV and 15 mA) which features a detection limit of 0.04°. X-ray photoelectron spectra (XPS) were recorded with a PHI 5400 XPS instrument equipped with an Al Kα source operated at 350 W and at 10^{-9} Torr. The nanoparticles were deposited onto a silicon wafer, and the spectra were charge-referenced to the Si 2p peak at 99.3 eV.

Electrochemistry. In a typical measurement, 1 mg of the Au−TiO_2 nanocomposite catalysts, 4 mg of carbon powder, and 10 μL of Nafion were ultrasonically mixed in 1 mL of methanol. Then 20 μL of this solution was transferred onto the glassy-carbon disk surface of a (gold) ring-(glassy-carbon) disk electrode (5.61 mm diameter, from Pine Instruments) with a Hamilton microliter syringe, corresponding to a catalyst loading of 20 μg (the respective gold mass loading was estimated to be 0.67 μg at x = 1.4%, 0.85 μg at x = 1.8%, 1.55 μg at x = 3.4%, 1.84 μg at x = 4.1%, 2.00 μg at x = 4.5%, 2.27 μg at x = 5.2%, 2.46 μg at x = 5.7%, and 2.73 μg at x = 6.4%). When the deposits were dried, 3 μL of Nafion was added to cover the electrode surface. Electrochemical assessments of the electrocatalytic activity in oxygen reduction were carried out in a standard three-electrode cell connected to a CHI 710C electrochemical workstation, with a Pt foil as the counter electrode and a reversible hydrogen electrode (RHE) as the reference electrode.

RESULTS AND DISCUSSION

Figure 1 shows the representative TEM micrographs of the series of Au−TiO_2 (x) nanocomposite particles at different Au/Ti atomic ratios: (a) x = 0%, (b) x = 1.4%, (c) x = 1.8%, (d) x = 3.4%, (e) x = 4.1%, (f) x = 4.5%, (g) x = 5.2%, (h) x = 5.7%, and (i) x = 6.4%. It can be seen that in all samples, whereas the TiO_2 nanoparticles exhibited apparent agglomeration forming a matrix of the order of a few hundred nanometers, individual nanoparticles can be rather clearly identified and the average diameter was estimated to be ca. 5 nm. For samples (b) to (i), the formation of Au nanoparticles was evidenced by the dark-contrast objects that were distributed on low-contrast TiO_2, with the diameter in the range of 10−50 nm. Additionally, high-resolution TEM measurements (Figure S2, Supporting Information) exhibited well-defined lattice fringes, where three lattice spacings can be estimated at ca. 0.39, 0.21, and 0.26 nm. The first one may be indexed to the (100) planes of anatase TiO_2,[24] whereas the last two are likely due to Au(200) and Au(111), respectively. This indicated the successful formation of Au−TiO_2 nanocomposites.

The formation of Au−TiO_2 nanocomposites was further manifested in XRD measurements. Figure 2 depicts the XRD patterns of the various Au−TiO_2 nanocomposites prepared above. From curve (a), it can be seen that the as-produced TiO_2 nanoparticles exhibited a series of well-defined diffraction peaks (filled squares) at 25.3°, 37.9°, 48.0°, 54.5°, and 62.8°, which may be assigned to the (101), (004), (200), (213), and (116) crystalline planes of anatase TiO_2 (JCPDS 75-1537). For samples (b) to (i), in addition to these diffraction features for anatase TiO_2, three new peaks (open circles) can be seen at 38.2°, 44.4°, and 64.6°, which are consistent with the (111), (200), and (220) crystalline planes of fcc gold. Furthermore, it can be seen that the gold diffraction features exhibited an apparent increase of intensity and concurrently a diminishment of the peak width, with increasing gold loading from curve (b) to (i). This can be ascribed to the increasing loading (size) of the gold nanoparticles. Note that the average diameter (τ) of the gold nanoparticles can be quantified by the Debye−Scherrer equation, $\tau = K\lambda/\beta \cos\theta$, where K is a dimensionless shape factor with a value of ~0.9; λ is the X-ray wavelength (1.54059 Å for Cu Kα); and β is the full width at half-maximum

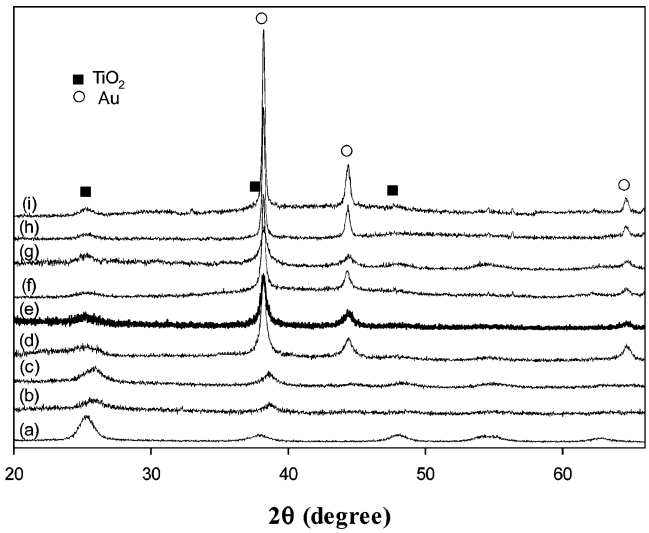

Figure 2. XRD patterns of Au−TiO_2 nanocomposites at different Au/Ti atomic ratios (x): (a) x = 0%, (b) x = 1.4%, (c) x = 1.8%, (d) x = 3.4%, (e) x = 4.1%, (f) x = 4.5%, (g) x = 5.2%, (h) x = 5.7%, and (i) x = 6.4%. Filled squares highlight the diffraction peaks of anatase TiO_2, and open circles signify those of Au.

(fwhm) of a selected diffraction peak. Therefore, based on the width of the Au(200) diffraction peak, the average diameter of the gold nanoparticles in the Au−TiO_2 nanocomposites was estimated, which showed an approximately linear increase with the Au/Ti atomic ratio (x): 10.4 nm at x = 1.8% (curve c), 13.4 nm at x = 3.4% (curve d), 14.8 nm at x = 4.1% (curve e), 16.2 nm at x = 4.5% (curve f), 18.0 nm at x = 5.2% (curve g), 19.5 nm at x = 5.7% (curve h), and 20.7 nm at x = 6.4% (curve i). The results are summarized in Table 1 and consistent with those observed in TEM measurements (Figure 1). For curve b (x = 1.4%), the gold diffraction features were not clearly defined, and hence no estimation was made.

Table 1. Summary of the Structures and Oxygen Reduction Activity of Au−TiO_2 Nanocomposites: Au/Ti Atomic Ratio (x), Gold Crystalline Domain Size (τ), Number of Electron Transfers (n) in Oxygen Reduction, Onset Potential (E_{onset}), and Kinetic Current Density (J_k)

x (%)	τ (nm)	n (at +0.60 V)	E_{onset} (V vs RHE)	J_k (A/m^2, at +0.70 V)
0		2.50	+0.74	4.6
1.4		2.81	+0.79	15.7
1.8	10.4	3.15	+0.82	15.6
3.4	13.4	3.14	+0.83	16.0
4.1	14.8	3.45	+0.85	14.0
4.5	16.2	3.70	+0.87	19.9
5.2	18.0	3.72	+0.88	63.7
5.7	19.5	3.56	+0.86	61.1
6.4	20.7	3.60	+0.83	13.8

The electrocatalytic activity of the Au−TiO_2 nanocomposites prepared above in oxygen reduction was then evaluated by voltammetric measurements. Figure 3 depicts the RRDE voltammograms of a glassy-carbon disk electrode modified with TiO_2 and Au−TiO_2 nanocomposites in an oxygen-saturated 0.1 M NaOH solution at varied electrode rotation rates (from 100 to 2500 rpm). It can be seen that in all samples nonzero cathodic currents started to appear when the electrode potential was swept negatively to about +0.8 V and reached a plateau at potentials more negative than +0.6 V, suggesting apparent electrocatalytic activity of the nanocomposites in oxygen reduction. In addition, the voltammetric currents collected at the ring electrode, where the potential was set at +1.4 V, were about an order of magnitude lower, indicating that only a minimal amount of peroxide intermediates was produced during oxygen reduction. However, a closer examination indicates that the catalytic performance varies rather drastically with the Au loading of the nanocomposites. For instance, for the electrode modified with TiO_2 nanoparticles alone (panel a), the limiting current (I_{lim}) at 2500 rpm was about 0.60 mA at +0.4 V; yet with the Au−TiO_2 nanocomposites (panels b to i), I_{lim} was markedly higher and varied with the Au/Ti atomic ratio (x): 0.60 mA at x = 1.4%, 0.62 mA at x = 1.8%, 0.96 mA at x = 3.4%, 1.04 mA at x = 4.1%, 0.95 mA at x = 4.5%, 1.24 mA at x =

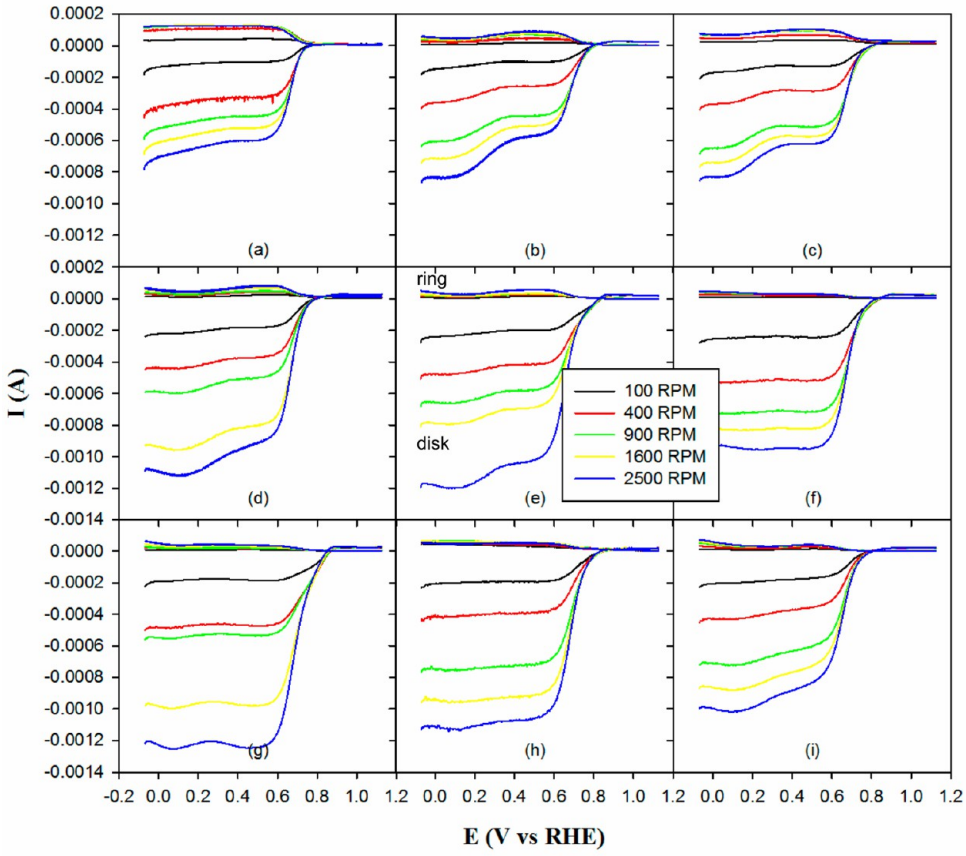

Figure 3. RRDE voltammograms of a glassy-carbon disk−gold ring electrode with the disk modified with (a) TiO_2, (b) Au−TiO_2 (1.4%), (c) Au−TiO_2 (1.8%), (d) Au−TiO_2 (3.4%), (e) Au−TiO_2 (4.1%), (f) Au−TiO_2 (4.5%), (g) Au−TiO_2 (5.2%), (h) Au−TiO_2 (5.7%), and (i) Au−TiO_2 (6.4%) in an oxygen-saturated 0.1 M NaOH solution. Electrode potential sweep rate was 10 mV/s, and the ring potential was set at +1.4 V. Nanocomposite loadings were all 20 μg.

5.2%, 1.07 mA at x = 5.7%, and 0.88 mA at x = 6.4%. That is, within the present experimental context, the Au−TiO_2 nanoparticles with the Au/Ti atomic ratio of 5.2% appeared to exhibit the best catalytic performance for oxygen reduction with the highest limiting currents (these observations also suggest only negligible contributions from carbon black, in comparison to those of the nanocomposites, to the observed ORR activity since the same amount of carbon black was added in the preparation of each catalyst ink, as detailed in the Experimental Section). This is further manifested in the analysis of the number of electron transfers (n) involved, onset potential, and kinetic current density in oxygen reduction, as detailed below.

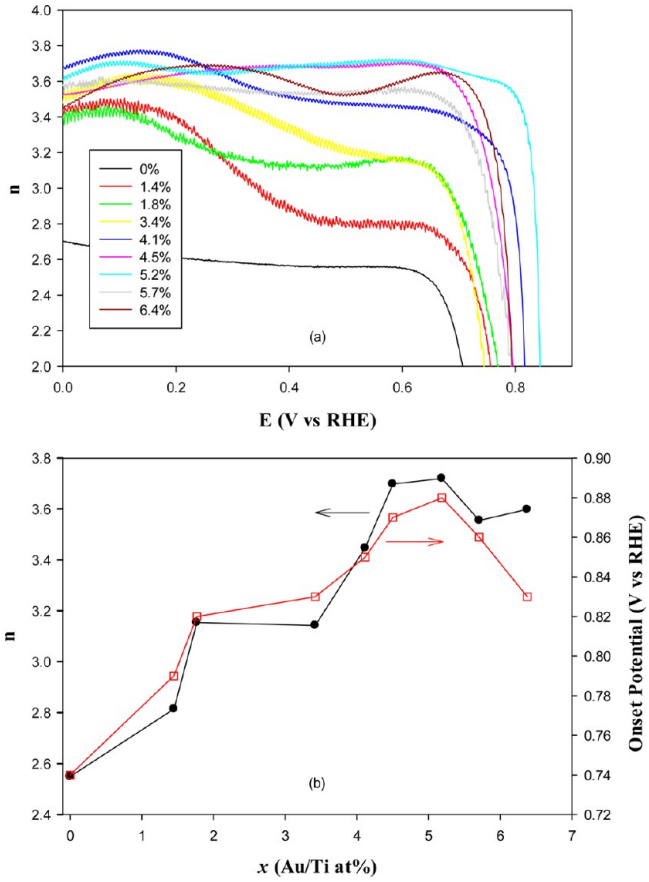

Figure 4. (a) Number of electron transfers (n) in oxygen reduction catalyzed by various Au−TiO_2 (x) nanocomposites. Data were calculated from the RRDE voltammograms at 2500 rpm in Figure 3. (b) Variation of the n value at +0.60 V (left y axis) and onset potential (right y axis) with the Au/Ti atomic ratio (x).

Figure 4(a) shows the number of electron transfers (n) in oxygen reduction at varied electrode potentials. The n values were calculated by

$$n = \frac{4I_D}{I_D + \frac{I_R}{N}} \quad (1)$$

where I_D and I_R denote the disk and ring currents, respectively, and N is the collection efficiency.[25] The RRDE voltammograms at 2500 rpm in Figure 3 were used for the estimations. One can see that for the TiO_2 nanoparticles (0%) the n values were mostly within a narrow range of 2.50−2.70 at potentials more negative than +0.70 V. In contrast, for Au−TiO_2 (x) nanocomposites, the n values were all markedly higher. For instance, at +0.60 V, the n values were 2.81 at x = 1.4%, 3.15 at x = 1.8%, 3.14 at x = 3.4%, 3.45 at x = 4.1%, 3.70 at x = 4.5, 3.72 at x = 5.2%, 3.56 at x = 5.7%, and 3.60 at x = 6.4%. The results are depicted by the filled circles in panel (b) (and summarized in Table 1). It is well-known that oxygen reduction in aqueous solutions typically occurs through two major pathways: the direct four-electron reduction pathway from O_2 to H_2O (i.e., n = 4) and the two-electron reduction pathway from O_2 to hydrogen peroxide (H_2O_2, n = 2).[26−28] Therefore, from this analysis, one can see that when oxygen reduction was catalyzed by TiO_2 alone peroxide derivatives constituted a major fraction of the reaction products, indicating that TiO_2 nanoparticles only had a limited catalytic activity. In contrast, for the series of Au−TiO_2 nanocomposites, the catalytic activity was markedly enhanced where the n values were primarily in the range of 3−4, with the highest one observed with the x = 5.2% sample at n = 3.72. This signifies that water was the primary reaction product of oxygen reduction.

It should be noted that with a loading of 20 μg of nanocomposites in the present study the thickness of the catalyst layers on the glassy carbon electrode surface was estimated to be less than 1 μm. Thus, minimal contributions are anticipated from nonelectrochemical decomposition of peroxide intermediates ($H_2O_2 \rightarrow H_2O + 1/2O_2$) to the quantitative estimation of the apparent number of electron transfers in ORR.[29] It has been found that for much thicker catalyst layers (>5 μm) peroxide species might be trapped within the matrix for a significant period of time and undergo decomposition nonelectrochemically.[30]

A similar behavior was observed with the onset potential of oxygen reduction, another critical parameter in the quantitative assessments of the electrocatalytic performance. From panel (a), this was defined as the crossing point between the rising part and the flat part of the n values. The results are plotted with the red squares in panel (b). It can be seen that in comparison to TiO_2 nanoparticles alone where the onset potential was estimated to be ca. +0.74 V the Au−TiO_2 nanocomposites all showed an onset potential that was significantly more positive, indicating that the addition of gold nanoparticles enhanced the electrocatalytic activity in oxygen reduction. Interestingly, the onset potential initially showed a rather monotonic shift in the positive direction with increasing gold content (x), reached the maximum of +0.88 V at x = 5.2%, and declined somewhat with a further increase of the x value. This observation again suggests that the Au−TiO_2 (5.2%) nanocomposites stood out as the best electrocatalysts among the series in oxygen reduction. Note that in a previous study where gold was potentiodynamically deposited onto a titanium electrode surface,[21] the resulting Au/TiO_2 composites were found to catalyze oxygen reduction via the 4e route in 0.1 M NaOH, with a very comparable onset potential at ca. +0.87 V (vs RHE).

Analysis of the electron-transfer kinetics also showed that the Au−TiO_2 (5.2%) nanocomposite exhibited the best catalytic activity in oxygen reduction. Note that the disk currents (I_D) entailed both diffusion (I_d) and kinetically controlled (I_k) components, as reflected by the Koutecky−Levich equation

$$\frac{1}{I_D} = \frac{1}{I_k} + \frac{1}{I_d} = \frac{1}{I_k} + \frac{1}{0.62nAFC_O D_O^{2/3} \nu^{-1/6} \omega^{1/2}} \quad (2)$$

where F is the Faradaic constant (96 500 C/mol), D_O the diffusion coefficient of O_2 (1.9×10^{-5} cm^2/s), ν the kinematic viscosity of the solution (9.97×10^{-5} cm^2/s), C_O the oxygen concentration in O_2-saturated solution (1.38×10^{-3} M), ω the rotation rate of the electrode, and A the area of the electrode. From linear regressions of the Koutecky–Levich plots of I_D^{-1} vs $\omega^{-1/2}$, the kinetic currents (I_k) may be quantified from the y-axis intercepts (not shown). Figure 5 depicts the Tafel plot of

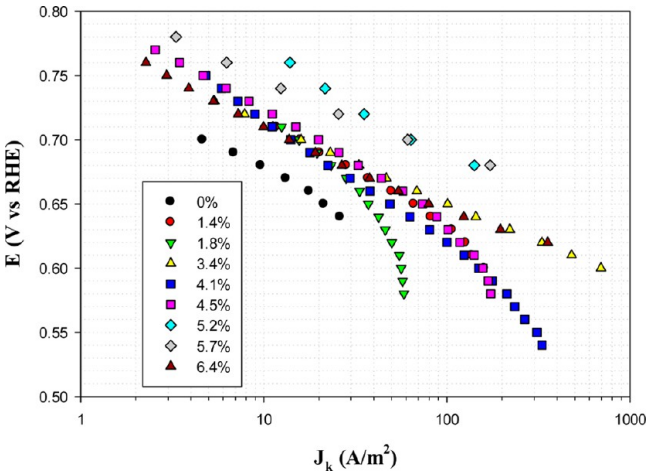

Figure 5. Variation of kinetic current density with electrode potential for oxygen reduction catalyzed by Au–TiO_2 (x) nanocomposites. Data were obtained from Koutecky–Levich analysis of the RRDE voltammograms in Figure 3.

the variation of the kinetic current density (J_k, I_k normalized by the electrode geometrical surface area) with electrode potential for the series of Au–TiO_2 nanocomposites. It can be seen that all nanocomposite catalysts exhibited a clear increase of the kinetic current density with increasingly negative electrode potential, and more importantly, the loading of gold nanoparticles into the nanocomposites markedly enhanced the electrocatalytic activity. For instance, the kinetic current density at +0.70 V is only 4.6 A/m^2 with TiO_2 alone but increases substantially to 15.7 A/m^2 with Au–TiO_2 (x = 1.4%), 15.6 A/m^2 at x = 1.8%, 16.0 A/m^2 at x = 3.4%, 14.0 A/m^2 at x = 4.1%, 19.9 A/m^2 at x = 4.5%, 63.7 A/m^2 at x = 5.2%, 61.1 A/m^2 at x = 5.7%, and 13.8 A/m^2 at x = 6.4% (Table 1). Furthermore, when normalized to the corresponding gold loading, the respective mass activity was found to be 581, 453, 255, 188, 246, 692, 612, and 125 A/g. In both analyses, the optimal gold loading among the series of nanocomposite catalysts appeared to be in the narrow range of 5.2–5.7% where the current density was more than 10 times higher than that with TiO_2 alone.

In addition, one can see that the slopes of the Tafel plot are all close to 60 mV/dec in the low overpotential region. This suggests that a pseudo two-electron reaction was likely the rate-determining step in the electrocatalytic reduction of oxygen following an outer-sphere electron-transfer pathway.[31] In this mechanism,[32,33] oxygen is solvated with water molecules forming $[O_2 \cdot (H_2O)_x]$ clusters, which then interact with adsorbed hydroxyl species (OH*) to promote a two-electron reaction route to form HO_2^- anions, and the HO_2^- anions may desorb from the disk electrode surface and be detected in the ring electrode or be further reduced with two additional electrons to OH^-. The reactions may be summarized as follows

$$[O_2 \cdot (H_2O)_x] + OH^* + e \rightarrow OH^* + OH_2^* + OH^- + [H_2O]_{x-1} \quad (3a)$$

$$HO_2^* + e \rightarrow HO_2^{-*} \quad (3b)$$

$$HO_2^{-*} \rightarrow HO_2^- \quad (3c)$$

$$HO_2^{-*} + H_2O + 2e \rightarrow 3OH^- \quad (3d)$$

In such a reaction mechanism, the effective number of electron transfers (n) is anticipated to be less than 4, as observed experimentally (Figure 4). Furthermore, presumably this reaction pathway is favored in the potential region where adsorption of hydroxyl groups to the metal surface is facilitated (more details below). In fact, XPS measurements of the Au–TiO_2 nanocomposites showed two peaks at ca. 530 and 532 eV, which were assigned to the 1s electrons of oxygen in TiO_2 and hydroxy (OH) moieties, respectively,[34] and the OH content was found to increase roughly with increasing gold loading in the nanocomposites (Figure S3, Supporting Information). This implies the promoting effects of gold nanoparticles in forming surface OH groups. Importantly, the fact that the optimal electrocatalytic activity was observed near x = 5.2% indicates that too high a concentration of OH groups may impede oxygen reduction likely as a result of steric blocking of oxygen adsorption onto the catalyst surface.

Taken together, the results presented above suggest that the Au–TiO_2 nanocomposites exhibited effective electrocatalytic activity in oxygen reduction, which might be attributed to the hypo-d-electron characters of titanium oxide that facilitated the intimate interactions with hyper-d-electron noble metals,[20,35] leading to effective spillover of adsorbed hydroxy moieties from the hypo-d-electron oxide support at the Au–TiO_2 interface

$$Ti(OH)_4 + Au \rightarrow Ti(OH)_3^+ + Au\text{-}OH + e \quad (4)$$

$$Ti(OH)_3^+ + 2H_2O \rightarrow Ti(OH)_4 + H_3O^+ \quad (5)$$

In these, the reactions of the resulting Au–OH with oxygen constituted a critical step in oxygen reduction, consistent with the above Tafel results (Figure 5). Importantly, one may note that the overall performance was comparable to or even better than those reported in the literature based on oxide-supported gold nanoparticles for oxygen reduction. For instance, in a previous study with gold nanoparticles (diameter 15–35 nm) supported on agglomerated SnO_2,[36] the functional nanocomposites with various gold loadings also exhibited apparent electrocatalytic activity in oxygen reduction in alkaline media, and the most active catalyst among the series was identified with a gold loading of 1.9 at. % where n was estimated to be 4.1 and the onset potential was around +1.0 V.

CONCLUSIONS

In this study, a series of Au–TiO_2 nanocomposites were successfully prepared by hydrothermal methods where gold nanoparticles were chemically grown onto TiO_2 nanocolloid agglomerates. Whereas the gold nanoparticles were relatively large in the range of 10–50 nm in diameter, the resulting Au–TiO_2 nanocomposites exhibited apparent catalytic activity for ORR in alkaline solutions. It was found that in comparison to TiO_2 alone the addition of gold nanoparticles markedly enhanced the ORR activity, as manifested in the increase of the n values from about 2.5 up to 3.7, the anodic shift of the onset potential from +0.74 to +0.88 V, and more than an order

of magnitude increase of the kinetic current density. Among the series, the sample with a gold/titanium atomic ratio of 5.2% was found to exhibit the best catalytic performance. The enhanced oxygen reduction kinetics was ascribed to the dissociation of water and formation of surface-adsorbed hydroxyl moieties that was facilitated by the loading of gold nanoparticles onto the TiO_2 colloids.

■ ASSOCIATED CONTENT

Supporting Information

Representative high-resolution TEM image and XPS data of the Au−TiO_2 nanocomposites. This material is available free of charge via the Internet at http://pubs.acs.org.

■ AUTHOR INFORMATION

Corresponding Author

*E-mail: shaowei@ucsc.edu.

Notes

The authors declare no competing financial interest.

■ ACKNOWLEDGMENTS

This work was supported, in part, by the National Science Foundation (CHE − 1012258, CBET − 1258839, and CHE − 1265635). C.L. was partially supported by a research fellowship from the China Scholarship Council. TEM and XPS studies were carried out at the Molecular Foundry and National Center for Electron Microscopy, Lawrence Berkeley National Laboratory, as part of a user project.

■ REFERENCES

(1) Wang, B. *J. Power Sources* **2005**, *152* (1), 1−15.
(2) Liu, Y.; Ishihara, A.; Mitsushima, S.; Kamiya, N.; Ota, K. *J. Electrochem. Soc.* **2007**, *154* (7), B664−B669.
(3) Mentus, S. V. *Electrochim. Acta* **2004**, *50* (1), 27−32.
(4) Suntivich, J.; Gasteiger, H. A.; Yabuuchi, N.; Nakanishi, H.; Goodenough, J. B.; Shao-Horn, Y. *Nat. Chem.* **2011**, *3* (7), 546−550.
(5) Reeve, R. W.; Christensen, P. A.; Hamnett, A.; Haydock, S. A.; Roy, S. C. *J. Electrochem. Soc.* **1998**, *145* (10), 3463−3471.
(6) Liu, H. S.; Song, C. J.; Tang, Y. H.; Zhang, J. L.; Zhang, H. J. *Electrochim. Acta* **2007**, *52* (13), 4532−4538.
(7) Zhang, L.; Zhang, J. J.; Wilkinson, D. P.; Wang, H. J. *J. Power Sources* **2006**, *156* (2), 171−182.
(8) Holze, R.; Vogel, I.; Vielstich, W. *J. Electrochem. Soc.* **1986**, *133* (3), C115−C115.
(9) Poznyak, S. K.; Kokorin, A. I.; Kulak, A. I. *J. Electroanal. Chem.* **1998**, *442* (1−2), 99−105.
(10) Baez, V. B.; Graves, J. E.; Pletcher, D. *J. Electroanal. Chem.* **1992**, *340* (1−2), 273−286.
(11) Tsujiko, A.; Itoh, H.; Kisumi, T.; Shiga, A.; Murakoshi, K.; Nakato, Y. *J. Phys. Chem. B* **2002**, *106* (23), 5878−5885.
(12) Choi, Y. K.; Seo, S. S.; Chjo, K. H.; Choi, Q. W.; Park, S. M. *J. Electrochem. Soc.* **1992**, *139* (7), 1803−1807.
(13) Parkinson, B.; Decker, F.; Juliao, J. F.; Abramovich, M.; Chagas, H. C. *Electrochim. Acta* **1980**, *25* (5), 521−525.
(14) Kim, J. H.; Ishihara, A.; Mitsushima, S.; Kamiya, N.; Ota, K. I. *Electrochim. Acta* **2007**, *52* (7), 2492−2497.
(15) Mirkhalaf, F.; Tammeveski, K.; Schiffrin, D. J. *Phys. Chem. Chem. Phys.* **2009**, *11* (18), 3463.
(16) Prieto, A.; Hernéndez, J.; Herrero, E.; Feliu, J. M. *J. Solid State Electrochem.* **2003**, *7* (9), 599−606.
(17) Andoralov, V. M.; Tarasevich, M. R.; Tripachev, O. V. *Russ. J. Electrochem.* **2011**, *47* (12), 1327−1336.
(18) Thorum, M. S.; Anderson, C. A.; Hatch, J. J.; Campbell, A. S.; Marshall, N. M.; Zimmerman, S. C.; Lu, Y.; Gewirth, A. A. *J. Phys. Chem. Lett.* **2010**, *1* (15), 2251−2254.
(19) Park, Y.; Nam, S.; Oh, Y.; Choi, H.; Park, J.; Park, B. *J. Phys. Chem. C* **2011**, *115* (14), 7092−7096.
(20) Krstajic, N. V.; Vracar, L. M.; Neophytides, S. G.; Jaksic, J. M.; Murase, K.; Tunold, R.; Jaksic, M. M. *J. New Mater. Electrochem. Syst.* **2006**, *9* (2), 83−97.
(21) Jasin, D.; Abu-Rabi, A.; Mentus, S.; Jovanovic, D. *Electrochim. Acta* **2007**, *52* (13), 4581−4588.
(22) Macak, J. M.; Schmidt-Stein, F.; Schmuki, P. *Electrochem. Commun.* **2007**, *9* (7), 1783−1787.
(23) Song, Y.; Klivansky, L. M.; Liu, Y.; Chen, S. *Langmuir* **2011**, *27* (23), 14581−14588.
(24) Lin, C.; Song, Y.; Cao, L.; Chen, S. *Nanoscale* **2013**, *5* (11), 4986−4992.
(25) Zhou, Z. Y.; Kang, X. W.; Song, Y.; Chen, S. W. *Chem. Commun.* **2012**, *48* (28), 3391−3393.
(26) Katsounaros, I.; Schneider, W. B.; Meier, J. C.; Benedikt, U.; Biedermann, P. U.; Auer, A. A.; Mayrhofer, K. J. J. *Phys. Chem. Chem. Phys.* **2012**, *14* (20), 7384.
(27) Masa, J.; Ozoemena, K.; Schuhmann, W.; Zagal, J. H. *J. Porphyrins Phthalocyanines* **2012**, *16* (07n08), 761−784.
(28) Lim, D. H.; Wilcox, J. *J. Phys. Chem. C* **2012**, *116* (5), 3653−3660.
(29) Suntivich, J.; Gasteiger, H. A.; Yabuuchi, N.; Shao-Horn, Y. *J. Electrochem. Soc.* **2010**, *157* (8), B1263−B1268.
(30) Bonakdarpour, A.; Lefevre, M.; Yang, R. Z.; Jaouen, F.; Dahn, T.; Dodelet, J. P.; Dahn, J. R. *Electrochem. Solid State Lett.* **2008**, *11* (6), B105−B108.
(31) Zhang, J. *PEM fuel cell electrocatalysts and catalyst layers: fundamentals and applications*; Springer: London, 2008.
(32) Lipkowski, J.; Ross, P. N. *Electrocatalysis*; Wiley-VCH: New York, 1998.
(33) Ramaswamy, N.; Mukerjee, S. *Adv. Phys. Chem.* **2012**, *2012*, 1−17.
(34) Stefanov, P.; Shipochka, M.; Stefchev, P.; Raicheva, Z.; Lazarova, V.; Spassov, L. *J. Phys.: Condens. Ser.* **2008**, *100*, 012039−1.
(35) Selvarani, G.; Maheswari, S.; Sridhar, P.; Pitchumani, S.; Shukla, A. K. *J. Electrochem. Soc.* **2009**, *156* (11), B1354−B1360.
(36) Chen, W.; Ny, D.; Chen, S. W. *J. Power Sources* **2010**, *195* (2), 412−418.